
Determination of effective electric conductivity of UFG/PEI-composites considering quantum mechanical tunnelling effects

Master thesis by Sebastian Wissel (Student ID: 2570677)

Date of submission: May 25, 2023

1. Review: Prof. Dr. Bai-Xiang Xu
2. Review: Prof. Dr. Hongbin Zhang
Darmstadt



TECHNISCHE
UNIVERSITÄT
DARMSTADT

Materials and Earth
Sciences Department
Mechanik Funktionaler
Materialien

Erklärung zur Abschlussarbeit gemäß § 22 Abs. 7 und § 23 Abs. 7 APB der TU Darmstadt

Hiermit versichere ich, Sebastian Wissel, die vorliegende master thesis ohne Hilfe Dritter und nur mit den angegebenen Quellen und Hilfsmitteln angefertigt zu haben. Alle Stellen, die Quellen entnommen wurden, sind als solche kenntlich gemacht worden. Diese Arbeit hat in gleicher oder ähnlicher Form noch keiner Prüfungsbehörde vorgelegen.

Mir ist bekannt, dass im Fall eines Plagiats (§ 38 Abs. 2 APB) ein Täuschungsversuch vorliegt, der dazu führt, dass die Arbeit mit 5,0 bewertet und damit ein Prüfungsversuch verbraucht wird. Abschlussarbeiten dürfen nur einmal wiederholt werden.

Bei der abgegebenen Thesis stimmen die schriftliche und die zur Archivierung eingereichte elektronische Fassung gemäß § 23 Abs. 7 APB überein.


Bei einer Thesis des Fachbereichs Architektur entspricht die eingereichte elektronische Fassung dem vorgestellten Modell und den vorgelegten Plänen.

Darmstadt, May 25, 2023

S. Wissel

Contents

1	Motivation	5
2	Basics	7
2.1	Quantum mechanics	7
2.1.1	Solution of the Schrödinger equation	8
2.1.2	Wave in infinite potential well	9
2.1.3	Wave towards finite potential wall	10
2.1.4	Electron tunnelling in 1d	12
2.2	Quantum-mechanical tunnelling effect	14
2.2.1	Geometrical considerations	14
2.2.2	Tunnelling at metal-semiconductor interfaces - Schottky contact . .	16
2.3	Percolation model for continuum	19
2.3.1	Transport exponents	19
2.3.2	Applied percolation model	20
2.3.3	Further percolation models	23
3	Documentation of the implemented model	24
3.1	Geometry and mesh generation	24
3.1.1	Geometry generation	24
3.1.2	Mesh generation	28
3.2	Input-file generation and MOOSE user element	28
3.3	Homogenization	29
3.4	Calculation spanning probability	31
4	Results	33
4.1	Verification of geometry generation	34
4.2	Analysis of potential and current density distributions	37
4.3	Effective conductivities	40
5	Conclusion	42



Calculations for this research were conducted on the Lichtenberg high performance computer of the TU Darmstadt.

Veröffentlicht unter CC-BY 4.0 International
<https://creativecommons.org/licenses/by/4.0/>

1 Motivation

The aim of this work is the development of a model to combine numerical simulations based on the finite element method (FEM) with quantum mechanical phenomena, like tunnelling. This is needed, since the importance of composites in mechanical and functional applications is increasing over the last decades. Especially the electrical properties of these materials are of interest, which are strongly influenced by tunnelling [1–13]. For a composite with insulating matrix material and little amount of high conducting inclusions, the effective conductance of the composite is most likely close to the conductance of the matrix material. This behaviour does not change for a small increase of the inclusions volume fraction, but changes drastically as soon as the amount of inclusion material comes close to a certain fraction. For volume fractions close or higher than this threshold, percolation occurs and the effective conductance jumps several orders of magnitude, close to the inclusions conductance. These switched electric properties often have a huge influence on the materials behaviour and might lead to a loss of applicability.

Fortunately, percolation is mainly a geometrical problem and the percolation thresholds are well documented for a plurality of different geometric shapes of inclusions. Due to their statistical approach of microstructure generation and simple implementation of physical interactions, the vast majority of numerical calculations is done via Monte-Carlo (MC) simulations [14–26]. Even though, most of the calculations are done with fully penetrable inclusions, there is also an approach with semi-penetrable inclusions [14], which will be used in this work. This is necessary, since in most simulations the length scale of inclusions and the decay length of the tunnelling process are equal. This is reasonable for microstructures with inclusions of a few nanometre, but is not maintainable for microstructures with inclusions of micrometre scale (decay length $\xi \approx \text{few nm}$). Such microstructures shall be investigated by FEM models in future.

Composites of micrometre scale are used for instance as coatings of metals to prevent corrosion and are applied in automotive industry to enable lightweight construction, but also in fuel tanks [27–29]. For the same purpose *Davidson et al.* investigated exfoliated, unfunctionalized graphite (UFG)-polyetherimide (PEI) composites, which is also the material combination treated in this work.

In the following, a model to implement tunnelling percolation in a finite element software, the corresponding geometry generation and distance calculation is presented. Aim is the validation of the model along literature values and the calculation of effective conductivities of example geometries.

2 Basics

In the following chapter a short introduction to the quantum mechanical tunnelling effect and its geometric properties are given. Also, an insight of percolation models is given.

2.1 Quantum mechanics

Since the establishment of quantum mechanics at the beginning of the 20th century and in particular the dissertation of Louis de Broglie 1924, matter is accounted to be both wave and particle [30]. This wave-particle duality replaced the view of the classical mechanics and could explain several physical issues, like Planck's law, the photoelectric effect or several years later the magnetism as part of the electromagnetism. One main difference of the quantum mechanics compared to classical mechanics is the uncertainty principle, which states that two conjugated variables of one particle can not be determined with arbitrary precision at the same time. The most famous conjugated variables are position and momentum. Nevertheless, Schrödinger was able to set up an equation which can describe quantum mechanical systems (equation 2.1). This function contains wavefunctions Ψ which can describe the time-dependent condition of a quantum mechanical state and the Hamiltonian \hat{H} .

$$i\hbar \frac{\partial}{\partial t} |\Psi(r, t)\rangle = \hat{H} |\Psi(r, t)\rangle \quad (2.1)$$

A special case of 2.1 is the time-independent Schrödinger equation, where the wavefunctions Ψ are just functions of the position and not time. Whereas these functions are mathematical expressions, their squared modulus is considered as the probability density to find a non-relativistic particle on position r at the given time.

2.1.1 Solution of the Schrödinger equation

The wave-particle duality is also valid for electrons, thus they can be described as wavefunctions Ψ . These wavefunctions can be described as superposition of plane waves. For waves with momentum $p = \hbar k$, wave vector $k = \frac{2\pi}{\lambda}$ and energy $E = \hbar\omega$, where ω is the frequency and λ the wave length, the plane wave function can be written as,

$$\Psi(r, t) = e^{i(kr - \omega t)}. \quad (2.2)$$

Differentiating and transformation of Ψ yields,

$$\begin{aligned} \frac{\partial \Psi}{\partial r} &= i \frac{p}{\hbar} \Psi \\ \frac{\partial^2 \Psi}{\partial r^2} &= -\frac{p^2}{2m_e} \Psi \\ p^2 &= -\frac{\hbar^2}{\Psi} \frac{\partial^2 \Psi}{\partial r^2} \end{aligned} \quad (2.3)$$

With the assumption, that the energy of the wave is the sum of its kinetic and potential energy ($E = \frac{p^2}{2m_e} + V$), the following Schrödinger equation is determined,

$$i\hbar \frac{\partial \Psi}{\partial t} = -\frac{\hbar^2}{2m_e} \frac{\partial^2 \Psi}{\partial r^2} + V\Psi. \quad (2.4)$$

If $V = V(r)$, separation of variables (equation 2.5) is used as an approach to solve equation 2.4. The functions Ψ and Φ are called eigenfunctions. Derivating Ψ lead to equations 2.6.

$$\Psi(r, t) = \Psi(r) \Phi(t) \quad (2.5)$$

$$\frac{\partial \Psi}{\partial t} = \Psi \frac{d\Phi}{dt} \quad (2.6)$$

$$\frac{\partial^2 \Psi}{\partial r^2} = \frac{d^2 \Psi}{dr^2} \Phi \quad (2.7)$$

Afterwards, the equation can be transformed into

$$\begin{aligned}
i\hbar\Psi\frac{d\Phi}{dt} &= -\frac{\hbar^2}{2m_e}\frac{d^2\Psi}{dr^2}\Phi + V\Psi\Phi \\
i\hbar\frac{1}{\Phi}\frac{d\Phi}{dt} &= -\frac{\hbar^2}{2m_e}\frac{1}{\Psi}\frac{d^2\Psi}{dr^2} + V.
\end{aligned}
\tag{2.8}$$

There the left side is just depending on t and the right side of r , thus both of them are constant. Introducing constant E , which is still the energy of the wave, leads to two equations:

$$\begin{aligned}
\frac{d\Phi}{dt} &= -\frac{iE}{\hbar}\Phi \\
E\Psi &= -\frac{\hbar^2}{2m_e}\frac{d^2\Psi}{dr^2} + V\Psi.
\end{aligned}
\tag{2.9}$$

Here, the second one is the time-independent Schrödinger equation and the factor $-\frac{\hbar^2}{2m_e}\frac{d^2}{dr^2} + V = \hat{H}$ is also known as Hamiltonian. The solution of the first equation is

$$\Phi(t) = e^{-i\frac{E}{\hbar}t}, \tag{2.10}$$

thus the solution of the Schrödinger equation looks like

$$\Psi(r, t) = \Psi(r) e^{-i\frac{E}{\hbar}t}. \tag{2.11}$$

An important fact is the time-dependence of Ψ , while the probability density has just a dependence on position r (equation 2.12).

$$|\Psi(r, t)|^2 = \Psi^*\Psi = \Psi^*e^{i\frac{Et}{\hbar}} \cdot \Psi e^{-i\frac{Et}{\hbar}} = |\Psi(r)|^2 \tag{2.12}$$

2.1.2 Wave in infinite potential well

Next step is the solution of the Schrödinger equation in a one dimensional potential well with infinitely high walls at a distance of a (see figure 2.1). Therefore the function is

examined step-by-step. Outside the walls the potential V is infinite, so the $\Psi(x)$ is zero. Inside the well V is zero, hence the time-independent part of equation 2.9 can be written as

$$-\frac{\hbar^2}{2m_e} \frac{d^2\Psi}{dx^2} = E\Psi \quad (2.13)$$

$$\frac{d^2\Psi}{dx^2} = -\frac{\sqrt{2m_e E}}{\hbar^2} \Psi = -k^2\Psi.$$

This is the equation of the harmonic oscillator and its solution has the structure

$$\Psi(x) = Ae^{ikx} + Be^{-ikx}, \quad (2.14)$$

Where A and B are constants which satisfy the boundary constraints 2.15. The terms of equation 2.14 represent two harmonic waves, which spread in opposite directions.

$$\Psi(x) \text{ has to be continuous} \rightarrow \Psi(0) = \Psi(a) = 0 \quad (2.15)$$

Hence, the first constraint delivers $B = -A$ and $A(e^{ika} - e^{-ika}) = 0$. Afterwards the solution of the second constraint gives two results. The trivial solution, where $A = 0$ and the general solution, where $ka = 0, \pm\pi, \pm2\pi, \pm3\pi, \dots$. Since $e^{ika} - e^{-ika} = 2i \sin(ika)$ and $\sin(ika)$ is zero for $k_n = n\frac{\pi}{a}$, with $n \in \mathbb{N}$. Thus k_n is defined, which also gives the values for E , which are shown in equation 2.16.

$$E_n = \frac{\hbar^2 k_n^2}{2m_e} = \frac{\pi^2 \hbar^2}{2m_e a^2} n^2 \quad (2.16)$$

2.1.3 Wave towards finite potential wall

Below, the case of a finite potential wall with height $V = V_0$ is considered. Therefore a wave is incoming towards the left side of a potential wall (see figure 2.2). If the energy of the wave E is larger than the potential V_0 , there is no distinct solution of equation 2.5 and interferences will be everywhere. In contrast, for $E < V_0$, the incoming wave has different momentums, for $x < 0$ it counts $p_1 = \hbar k_1$ and for $x > 0$ p_2 is presumed to be $\hbar k_2$. The kinetic energy K is also different. While $K = \frac{p_1^2}{2m_e} = E$ is presumed for $x < 0$, $K = \frac{p_2^2}{2m_e} = E - V_0$ is valid for $x > 0$. Thus,

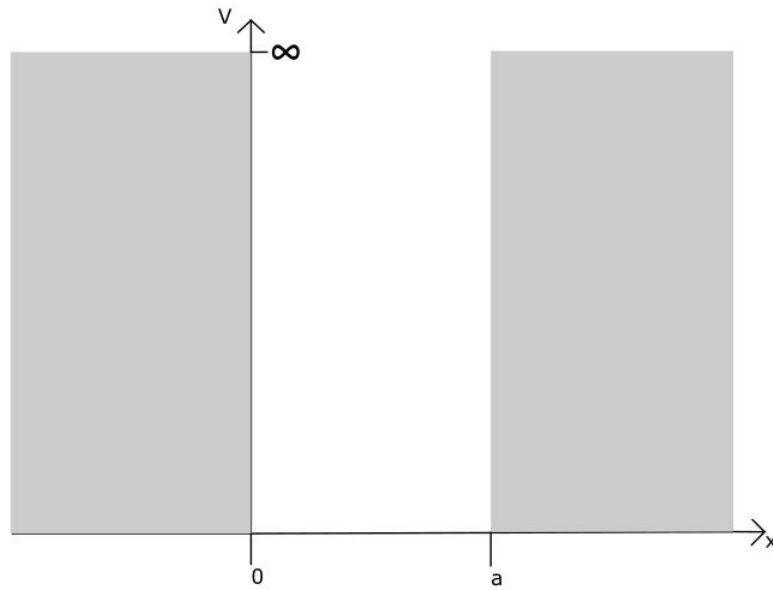


Figure 2.1: A one dimensional potential well with infinite high walls is shown.

$$\begin{aligned}
 k_1 &= \sqrt{\frac{2m_e E}{\hbar^2}} \\
 k_2 &= \sqrt{\frac{2m_e (E - V_0)}{\hbar^2}}.
 \end{aligned}
 \tag{2.17}$$

As in chapter 2.1.2 Ψ has to be continuous. In addition, also $\frac{\partial \Psi}{\partial x}$ has to be continuous, hence, $\Psi(0) = \frac{\partial \Psi(0)}{\partial x}$. The eigenfunction Ψ for $x < 0$ consists of two waves, one spreading wave towards the positive direction of the x-axis and one towards the negative direction and is considered as reflected wave. Their amplitudes are A_1 and A'_1 and both have the same momentum p_1 . However, there is only one transmitted wave in the area $x > 0$ with Amplitude A_2 and momentum p_2 . While k_1 is always a real number, k_2 is imaginary for $V_0 > E$. Thus the probability density decreases exponentially in this case.

To evaluate the transmission of the system, equation 2.14 is solved with regards to its constraints. The first constraint delivers $ik_2 A_2 = ik_1 (A_1 - A'_1)$, while the second one gives the correlation $A_2 = A_1 + A'_1$. Introducing the reflexion coefficient R and the transmission coefficient T , transforming the previous relations yield,

$$\frac{A'_1}{A_1} = \frac{k_1 - k_2}{k_1 + k_2} \quad (2.18)$$

$$\frac{A_2}{A_1} = \frac{2k_1}{k_1 + k_2} \quad (2.19)$$

$$R = \left| \frac{A'_1}{A_1} \right|^2 \quad (2.20)$$

$$T = \frac{k_2 + k_2^*}{2k_1} \left| \frac{A_2}{A_1} \right|^2. \quad (2.21)$$

For R and T the relation $R + T = 1$ must be valid.

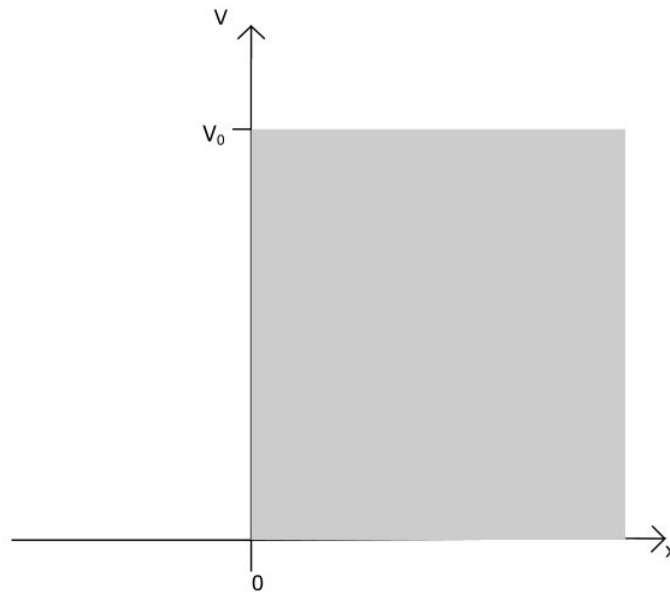


Figure 2.2: A one dimensional potential wall with finite height V_0 is shown.

2.1.4 Electron tunnelling in 1d

After the treatment of finite potential walls, a further expansion of the model to thin

potential walls is done. The potential wall of chapter 2.1.3 is reduced to a thickness a (see figure 2.3). Like in the previous chapter Ψ and $\frac{\partial\Psi}{\partial x}$ have to be continuous. Eigenfunction Ψ is defined in sections as,

$$\begin{aligned}\Psi_1(x) &= A_1 e^{ik_1 x} + A_1' e^{-ik_1 x} & \text{for } x < 0 \\ \Psi_2(x) &= A_2 e^{ik_2 x} + A_2' e^{-ik_2 x} & \text{for } 0 \leq x \leq a \\ \Psi_3(x) &= A_3 e^{ik_3 x} + A_3' e^{-ik_3 x} & \text{for } x > a.\end{aligned}\quad (2.22)$$

Since, $V(x < 0) = V(x > a) = 0$ the wave numbers in section 1 and 3 have to be equal ($k_1 = k_3$). Also, the continuous constraints

$$\begin{aligned}\Psi_1(0) &= \Psi_2(0) \\ \frac{\partial\Psi_1(0)}{\partial x} &= \frac{\partial\Psi_2(0)}{\partial x} \\ \Psi_2(a) &= \Psi_3(a) \\ \frac{\partial\Psi_2(a)}{\partial x} &= \frac{\partial\Psi_3(a)}{\partial x}\end{aligned}\quad (2.23)$$

have to be satisfied. For an incoming wave from the left side, A_1 is arbitrary, while $A_3' = 0$ since there is no incoming wave from the right side. These assumptions yield the equations for the wave vectors

$$\begin{aligned}k_1 = k_3 &= \sqrt{\frac{2m_e E}{\hbar^2}} & \text{for } x < 0 \vee x > a \\ k_2 &= \sqrt{\frac{2m_e (E - V_0)}{\hbar^2}} & \text{for } 0 \leq x \leq a.\end{aligned}\quad (2.24)$$

After several transformation with the assumption of $E < V_0$, the reflection coefficient R and the transmission coefficient T can be calculated with the equations 2.25.

$$\begin{aligned}R &= \frac{4E(V_0 - E)}{4E(E - V_0) - V_0^2 \sinh^2\left(\sqrt{2m_e(V_0 - E)}\frac{a}{\hbar}\right)} + 1 \\ T &= \frac{4E(E - V_0)}{4E(E - V_0) - V_0^2 \sinh^2\left(\sqrt{2m_e(V_0 - E)}\frac{a}{\hbar}\right)} \\ T &\sim \frac{16E(V_0 - E)}{V_0^2} e^{-2\sqrt{2m_e(V_0 - E)}\frac{a}{\hbar}}\end{aligned}\quad (2.25)$$

Due to clarity issues an example calculation of T is done with the parameters $E = 1eV$, $a = 100pm$ and $V_0 = 2eV$. An electron in this setup has a finite transmission probability of 0.64. Hence, electrons can pass potential barriers, even if their energy is smaller than the potential walls energy. Also, for small electron energies, their transmission probability is decent, if the potential barrier is thin enough [25, 31–34].

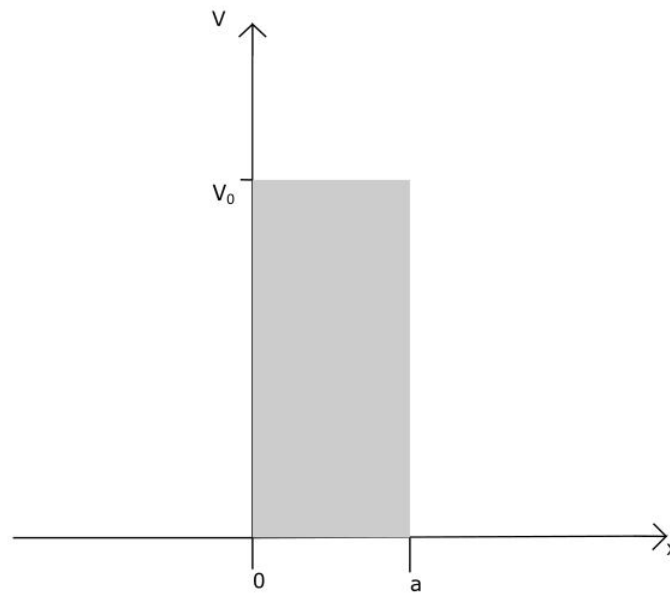


Figure 2.3: A one dimensional potential wall with finite height V_0 and thickness a is shown.

2.2 Quantum-mechanical tunnelling effect

2.2.1 Geometrical considerations

After the theoretical discussion of the tunnelling effect, the focus is shifted to its geometrical properties. As shown in chapter 2.1.4, it is possible for electrons to pass a potential barrier with higher energy than its own. Since the Schrödinger equation is radially symmetric, tunnelling is non-directional from a theoretical point of view. This simplifies the geometric

modelling, since only the shortest distances between inclusions have to be considered. As shown in the following chapter 2.3, the percolation models predict the same, due to the expectation, that the conduction between nearest neighbours will be the dominant contribution to the local conductivity of the composite.

Another important factor on the tunnelling possibility is the potential barrier height, which depends on the shape of the potential well along the tunnelling junction. External electric fields change this shape since they decrease the potential barrier in potential direction and increase it in the opposite direction. In figure 2.4 the change of the Coulomb potential well due to a strong external field is shown schematically. There, the potential energy V_0 is named as E_b and the tunnelling distance L is the difference between position X_2 and X_1 [35]. The change is directly influenced by the potential difference. This effect is utilised at the excitation of matter with LASERS [36, 37] or in the field emission gun in scanning electron microscopes [38–40]. Nevertheless, it is neglected in percolation models, since the spatial dependence is considered to be the dominant factor (see also ??).

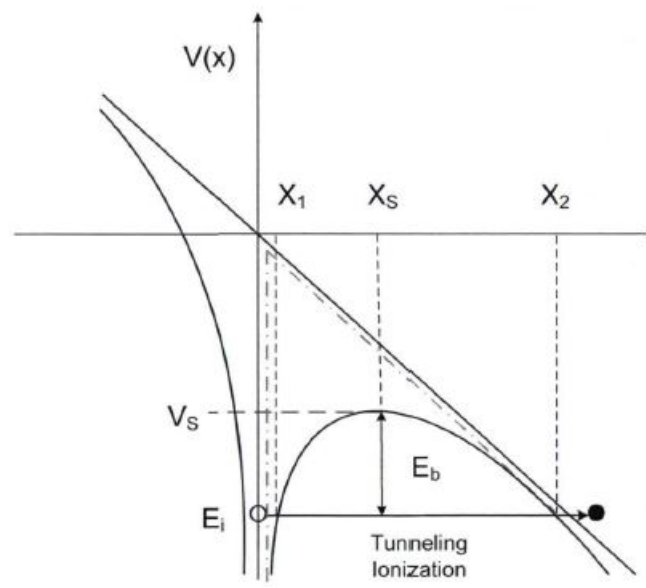


Figure 2.4: Schematic diagram of bending a Coulomb potential well by a strong external field [35].

2.2.2 Tunnelling at metal-semiconductor interfaces - Schottky contact

In the following chapter, the shape of the potential wall in the present microstructure is discussed. Therefore the band diagrams of metals and n-doped semiconductors are investigated (see figure 2.5). As shown there, the band structure of metals is quite simply. Their conduction and valance band overlap, hence the Fermi energy $E_{F,M}$ is equal to the highest occupied state at a temperature of 0 K. To ionize the metal, the energy of an electron has to be increased up to the vacuum energy E_{vac} . Also, the work function ϕ , ionisation energy I_P and electron affinity χ are equal. In contrast, the conduction and valance band of a semiconductor do not overlap. Therefore there are no possible states in a distinct energy region. This energy region reaches from the highest occupied state in the valance band (*HOMO*) with energy E_{VB} , to the lowest unoccupied state in the conduction band (*LUMO*) with energy E_{CB} . The energy difference of *HOMO* and *LUMO* is also known as bandgap $E_g = E_{CB} - E_{VB}$. On the right side of figure 2.5 an n-doped semiconductor is shown. N-doped semiconductor are doped with donators, which increase the number of valance electrons. For a silicon semiconductor, phosphor can be used as a donator, because this element has five valance electrons instead of the four silicon valance electrons. But also dangling bonds, surface states (due to breaking the crystal symmetry or absorbed species), adsorbed species and coatings lead to a local change of a semiconductors bandstructure. Like doping, it influences the position of the semiconductors Fermi energy $E_{F,SC}$. In case of an undoped semiconductor $E_{F,SC}$ is in the middle of the bandgap, thus $E_{F,SC} = E_{VB} + \frac{E_g}{2}$. This is also valid for a n-doped semiconductor at $T = 0$ K. For increasing temperatures $E_{F,SC}$ shifts to higher energies, depending on the donator concentration N_D . Furthermore, ϕ , χ and I_P are not equal. Nevertheless, they can be calculated with the equations 2.26. [41]

$$\phi = E_{vac} - E_{F,SC} \quad (2.26)$$

$$\chi = E_{vac} - E_{CB} \quad (2.27)$$

$$I_P = E_{vac} - E_{VB} \quad (2.28)$$

The connection of metal with an n-doped semiconductor occurs in four steps. Before contact, their energies have their material-dependent values. If the metal is connected to the semiconductor, as first step their Fermi energies are adapted, which means there is an electron exchange. This leads to a difference of the vacuum energies, which has the value $eV_{d,n}$ and is shown on the top right of figure 2.6. Afterwards, the vacuum energies E_{vac} are aligned, which leads to a difference in the Fermi energies, which is called $\Phi_{B,n}$. From

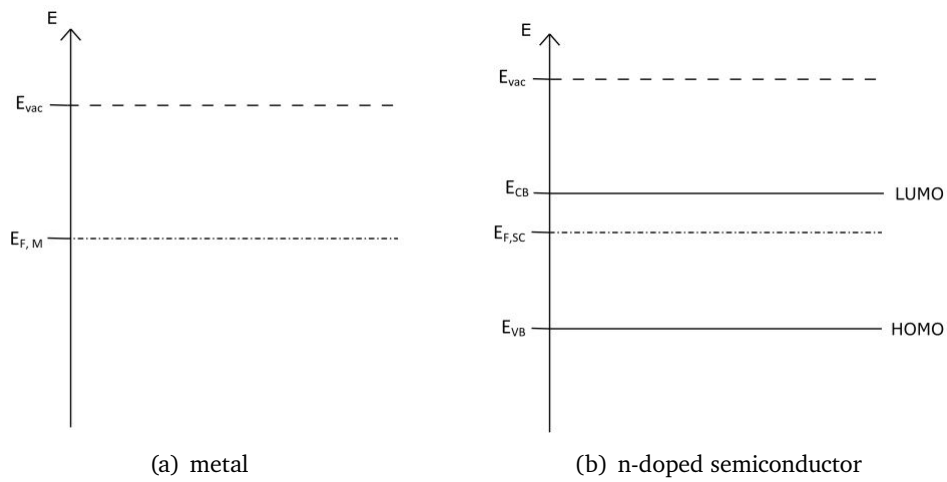


Figure 2.5: The figure shows typical band diagrams of a metal and a n-doped semiconductor.

now on E_{vac} of the semiconductor and the energies E_{CB} and E_{VB} have defined values at the interface. As the last step, the Fermi energies are adjusted by electron exchange between the materials. This leads to band bending in the semiconductor. The depleted area in the semiconductor, with thickness W , is called space charge layer (see figures 2.5 and 2.6). [41]

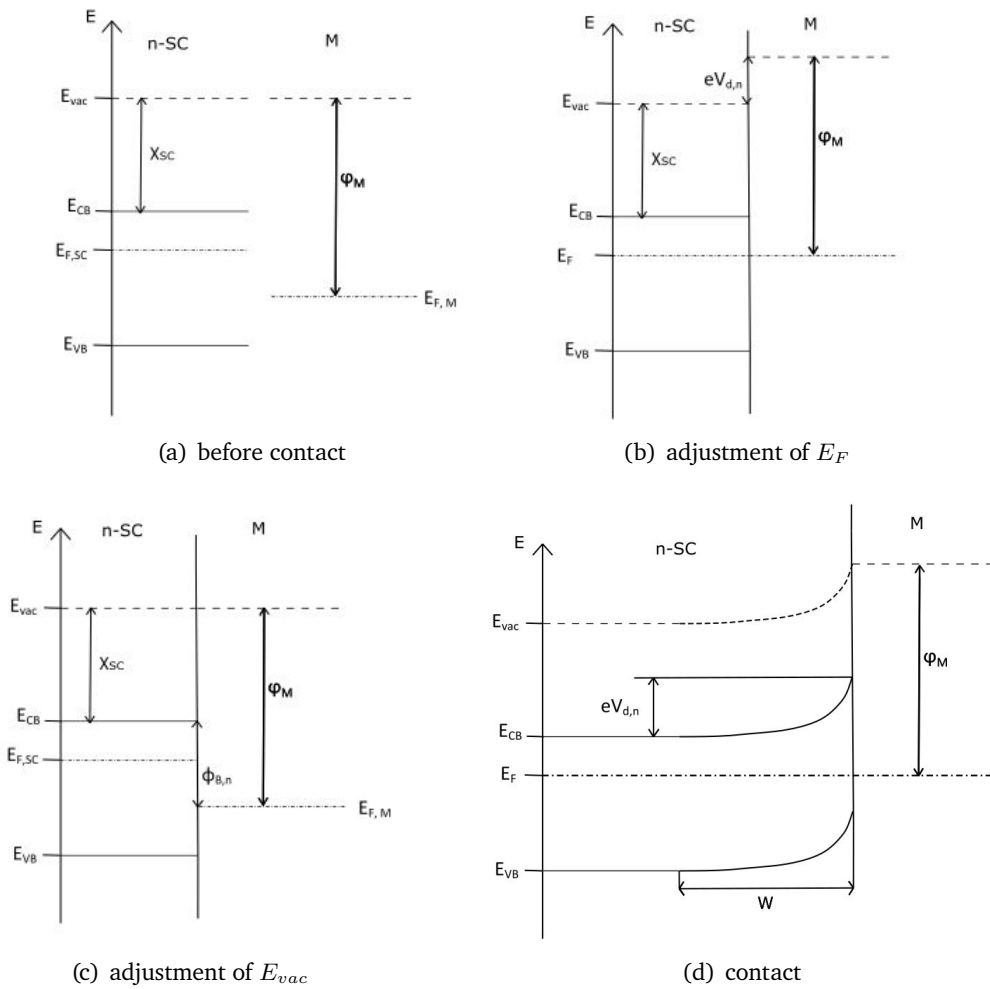


Figure 2.6: The adjustment of energies while the connection of a n-doped semiconductor with a metal is shown.

2.3 Percolation model for continuum

According to *Aharony et al.* and *Johner et al.* [14, 42] the electric properties of an disordered conductor-insulator composite switch from insulating to conducting, as soon as at least one macroscopic path of charge carriers spans the whole sample. This percolation paths can be arranged as direct or indirect connections. Whereat overlap of inclusions is considered as direct and quantum mechanical tunnelling connections as indirect contact. For inclusions of the same size, the percolation threshold η_c , so the critical density of inclusions at which 50% of comparable microstructures have at least one percolation path, decreases heavily, if tunnelling occurs. As an example, for a microstructure with almost every particle connected via tunnelling η_c is around 0.34. Whereas for microstructures with only direct connections η_c rises to 0.45 [14].

2.3.1 Transport exponents

As investigated in several publications [14, 43–45], the macroscopic conductance G of a direct-contact composite follows the power-law behaviour

$$G = G_0 (x - x_c)^t \quad (2.29)$$

with G_0 as proportionality constant, x as the concentration of the conducting phase, x_c as the volume concentration at the percolation threshold and transport critical exponent t [14]. For concentrations near the critical concentration, so $x - x_c \ll 1$, t is almost universal, with $t = t_0 \sim 2.0$. As shown in [45] this universal value hold true for real systems, where t varies in the range of 1.5 up to 11. There were several approaches to explain this behaviour and also consider it in numerical simulations [14, 42, 46–49]. The publications agree that nonuniversality stems mainly from inclusion distribution differences. They establish particle and conductivity distribution functions $P(r)$ and $h(\sigma)$ (see eq. 2.30), where r is the distance between the inclusion midpoints. In equation 2.30 the mean distance between particles a and the tunnelling decay factor ξ are used to calculate the proportionality factor α (eq. 2.31).

$$\begin{aligned} P(r) &\sim \exp\left(-\frac{r}{a}\right) \\ h(\sigma) &\sim \sigma^{-\alpha} \end{aligned} \quad (2.30)$$

$$\alpha = 1 - \frac{\xi}{2a} \quad (2.31)$$

As shown by *Kogut et al.* [46] via effective medium approximation and later by *Stenull et al.* [48], the explicit form of the transport exponent looks like:

$$t = \begin{cases} t_0 & \text{for } \nu + \frac{1}{1-\alpha} \leq t_0 \\ \nu + \frac{1}{1-\alpha} & \text{for } \nu + \frac{1}{1-\alpha} > t_0, \end{cases} \quad (2.32)$$

$$(2.33)$$

with $\nu \sim 0.88$ as correlation length exponent [14, 42]. *Johner et al.* also verified the governance for both overlapping and nonoverlapping spheres, as both kind of systems show universal behaviour close to the percolation threshold and a concentration dependant transport exponent $t(x)$ for concentrations away from the percolation threshold x_c .

2.3.2 Applied percolation model

As indicated several times the percolation model applied in this work is based on the model presented by *Johner et al.* [14]. Microstructures in the present work consist of an insulating matrix material and high-conducting spherical inclusions. The spheres are semi-penetrable, which means they have an impenetrable core and a penetrable concentric shell. Φ is defined as core diameter, while the shell thickness is given by $\frac{R}{2}$, where R represents the cut-off radius. R is introduced to reduce the considered tunnelling connections of the microstructure, since the transmission probability T decreases rapidly with increasing distance between the spheres. Thus, spheres are only connected via tunnelling, if their shells overlap (see figure 2.7). The interparticle conduction $\sigma(r)$ is given by equation 2.34. Where σ_0 represents the contact conductance and ξ the characteristic tunnelling distance (also tunnelling decay length).

$$\sigma(r) = \sigma_0 \cdot e^{-\frac{2(r-\Phi)}{\xi}} \quad (2.34)$$

$$\xi = \frac{\hbar}{\sqrt{2m_e \Delta E}} \quad (2.35)$$

Especially in older percolation models, the energy dependence of tunnelling is completely neglected and σ_0 and ξ are only used as fitting parameters (see [14, 26, 44, 49]). In

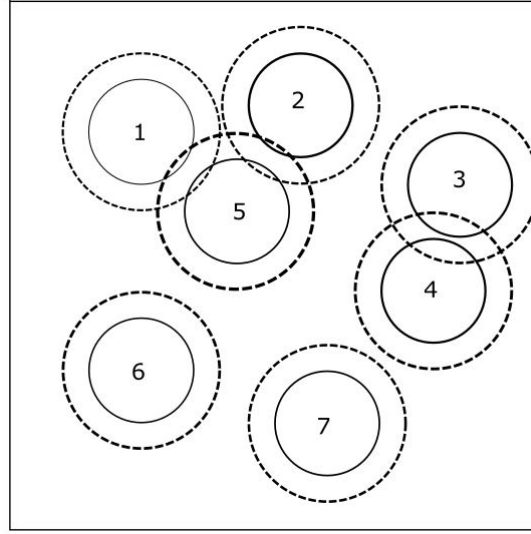


Figure 2.7: A two-dimensional visualization of semi-penetrable spheres is shown, where the solid lines visualize the impenetrable core and the dash lines the penetrable shell. If two shells overlap, tunnelling is applied.

contrast *Li et al.* [15] and furthermore *Hu et al.*, *Bao et al.* and *Kale et al.* improved the accuracy of equation 2.34 by deriving both parameters from quantum mechanics (see 2.1.4) [22, 25, 32]. Nevertheless, only the expression for the characteristic tunnelling length ξ is used in the present work (eq. 2.35, with electron mass m_e and potential barrier height ΔE). The reason for this is difficult approximation for σ_0 . Since for the transformation of the contact resistance $R_{contact}$ into a conductivity a minimum length between two particles is necessary. The approximation of this length is difficult since there are no known investigations about the inclusion materials behaviour in the used matrix material. For instance passivation layers or electrostatic interactions between the particles will have a huge influence on the minimal distance. Therefore σ_0 is a fixed value in the following calculations.

It is worth emphasising the importance of the cut-off radius R , which directly influences the appearance of a tunnelling flux between two particles (see eq. 2.37).

$$\sigma(r) = \begin{cases} \sigma_0 \exp\left(-\frac{2(r - \Phi)}{\xi}\right) & \text{for } (r - \Phi) \leq R \\ 0 & \text{for } (r - \Phi) > R \end{cases} \quad (2.36)$$

$$(2.37)$$

For the analysis of different microstructures an already mentioned parameter, called density η is introduced. η is a dimensionless quantity, which describes the volume fraction of the inclusion material and its shells. Therefore the number density $\rho = \frac{N}{V}$, with particle number N and composite volume V is used to calculate η (eq. 2.38). Since the tunnelling conduction is ruled by the overlap of the penetrable shells, obviously the volume of both parts of the inclusions have to be considered.

$$\eta = \rho \frac{\pi}{6} (\Phi + R)^3 \quad (2.38)$$

Also, the volume concentration x is calculated with ρ and core radius Φ (eq. 2.39). This leads to a relation between η and x , where a penetrability coefficient λ is introduced (eq. 2.40). [14]

$$x = \frac{\rho \pi \Phi^3}{6} \quad (2.39)$$

$$x = \lambda^3 \eta \quad (2.40)$$

$$\lambda = \frac{\Phi}{\Phi + R} \quad (2.41)$$

Furthermore, the spanning probability is introduced, which represents the probability that a percolation path occurs for an arbitrary number of likewise microstructures. Since they are used later, a fitting function for spanning probability- η graphs (eq. 2.42) with two fitting parameters $\eta_c(L)$ and $\Delta(L)$ is established, where L is the length of the system. For the critical density of a finite system $\eta_c(L)$ and the width of the percolation threshold $\Delta(L)$ the scaling relations 2.43 are valid, where η_c is the critical density for an infinite system and ν the correlation length exponent. [14, 42, 50]

$$\frac{1}{2} \left(1 + \tanh \left[\frac{\eta - \eta_c(L)}{\Delta(L)} \right] \right) \quad (2.42)$$

$$\eta_c(L) - \eta_c \propto L^{-\frac{1}{\nu}} \quad (2.43)$$

$$\Delta(L) \propto L^{-\frac{1}{\nu}} \quad (2.44)$$

2.3.3 Further percolation models

In addition to the previously presented models, there are several other approaches in literature, which won't be discussed here. Nevertheless, the author want to point out another common approach, which is based on Kirchhoff's current law. This model is often used in microstructures with inclusions with high aspect ratios, for example carbon nanotubes. Further insight give the publications of *Hu et al.* [32] and *Kogut et al.* [46]. Also the temperature dependence of the tunnelling process are investigated in [51–54], but will be neglected in this work, since the temperature for the examines microstructures is constant.

3 Documentation of the implemented model

In this chapter an overview of the written code and thus the implemented model is given. Several programs were used. First of all a *Python* code is used for automatic geometry- and input-file generation. The geometry-file is written for execution with the open source software *GMSH*, which is used to generate a mesh-file [55]. The finite element analysis is done with the open source software *Multiphysics Object-Orientated Simulation Environment*, short *MOOSE* [56, 57]. In the following, a description of the geometry and mesh generation, as well as a description of the *MOOSE* user element is given. Also, an insight on the applied homogenization method and a description of the spanning probability calculation is given.

3.1 Geometry and mesh generation

At first, the microstructure has to be generated this is done by using the software *GMSH*. Also, the mesh generation is done with *GMSH*. To get to this point a ".geo" file has to be written. This is done with a *Python* script to automate the microstructure generation and obtain flexibility for distinct parameters like the number of particles or their radius. In the following, the algorithm for the microstructure generation is elucidated and also the mesh generation within *GMSH* is clarified.

3.1.1 Geometry generation

As explained in the previous paragraph, the microstructure generation is done by executing

a *Python* script. In this section, its structure and the used functions are explained. To improve the clarity of the algorithm, the code is shown in as a flow chart in figure 3.1. The microstructure itself shall be a composite with randomly and uniformly distributed spherical inclusions. Unfortunately, the microstructure generation with thin cuboids as inclusions, does not work fully. Since there is still an overlap between some particles, the geometry can not be meshed with *GMSH*. Even though, the microstructures would still represent real physical systems.

Due to the parametrised functions used in the script “generation_geo_input.py”, some global defined parameters have to be introduced. At first, the geometrical parameters are defined. Starting with the relation between radius and bounding box length r_{PhiL} and number of particles *number*, it has to be decided which kind of inclusions should be implemented. As mentioned before the options are “spheres” or “flakes”, for the latter one, thin cuboids will be implemented. Afterwards, the radius of the “spheres” and length, width and height of the “flakes” have to be given. Notice, if the influence of the particle shape should be investigated, the radius of the sphere should be dependent on the cuboids geometrical parameters to ensure a better comparability. It is recommended the fit the radius in such a way, that both inclusions have the same volume. Furthermore cut-off radius (dependent on desired λ value), tunnelling decay length (material-dependent), radius of the tunnelling surfaces (will be explained in section ??), potential direction and the material conductivities have to be defined.

The actual calculations start with the generation of a microstructure with *number* of inclusions (see 3.1). Here, the overlap with other inclusions is not allowed, so if the core of one particle intersect with the core of another one, new coordinates are generated. For coordinate generation in each direction, the “numpy.random.uniform()” function of the *Python* fundamental package *NumPy* is used. As soon as the positions of all inclusions are calculated, the *GMSH* command instructions for the generation of the bounding box and the inclusions are saved. In the next step the distance between each particle combination and also between top and bottom surface (for potential in z -direction) are calculated and evaluated, if tunnelling can occur. Therefore the distance is evaluated with the help of the cut-off radius. This geometrical evaluation follows the constraints of equation 2.37. In the next step, the positions of tunnelling surfaces are calculated. This is necessary, since *MOOSE* does not provide a connection mechanism for nodes, which are not nearest neighbours of each other. Such an mechanism only exists for surfaces. It is called *ThermalContact*. As mentioned before, *GMSH* does not allow an overlap between surfaces, thus the tunnelling surfaces have to be shifted towards the midpoint of the corresponding inclusion. Therefore, the distance between actual tunnelling point and midpoint is scaled with an factor of 0.90. This ensures both, the ability to mesh the geometry and maintaining

physical reasonability, since the potential is almost constant inside a particle, due to its large conductivity. Before the tunnelling surface and volume command instructions for *GMSH* can be saved, the tunnelling surfaces have to be embedded in the corresponding inclusions, to ensure connection between them, also inside the mesh. Otherwise, *MOOSE* might not find them. These steps are followed by the determination of so called *physical entities*, this is an option of *GMSH* to assign different parts of the geometry distinct entities, which will also be saved in the mesh. This enables the possibility to assign distinct geometrical features, like surfaces or volumes, different properties. As last steps, the characteristic lengths, which are important for meshing the geometry, are defined and the gap conductivities for each tunnelling junction are calculated, before the “.geo”- and “tunnellingList.txt”-file are written.

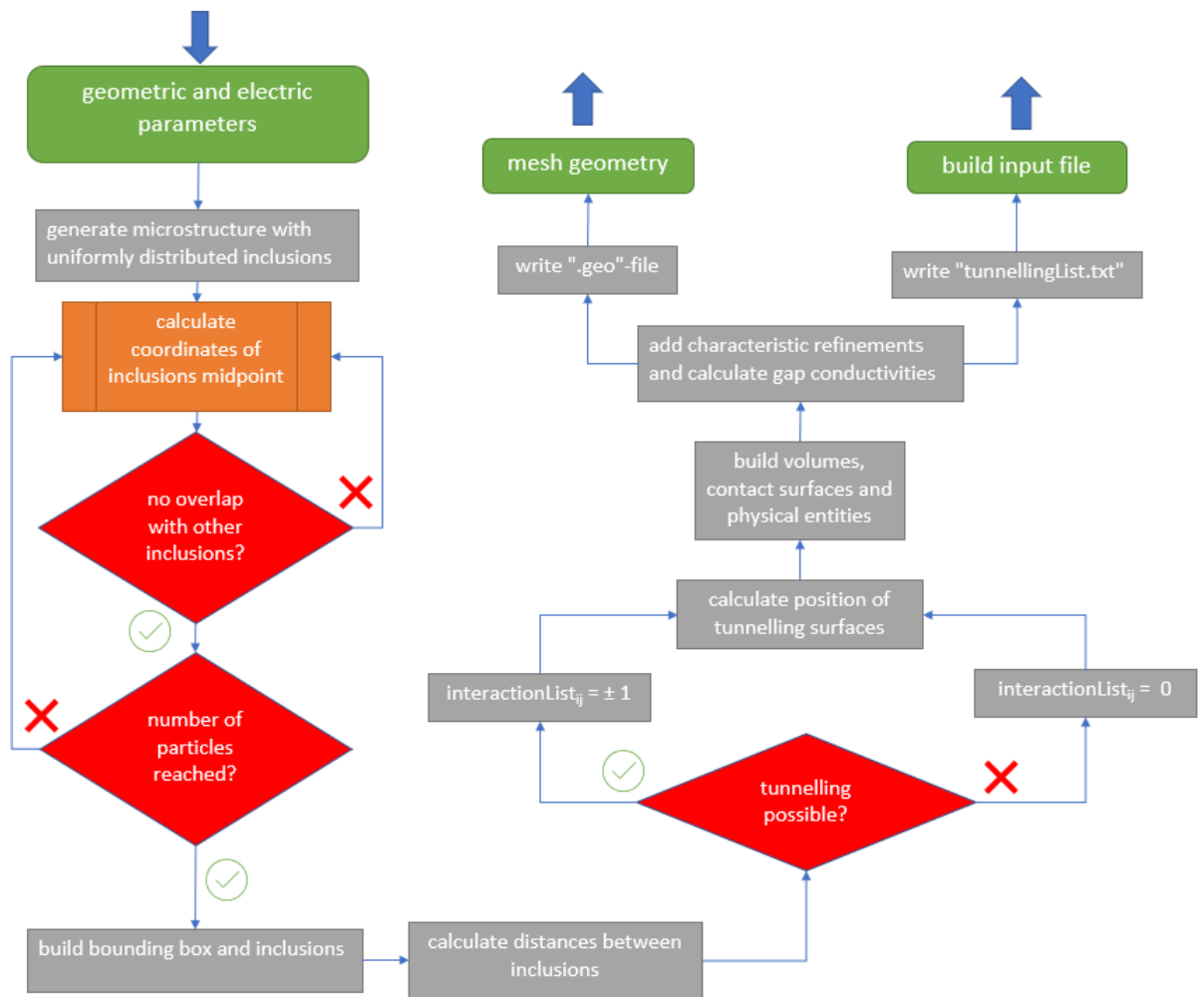


Figure 3.1: The flow chart of the geometry generation is shown.

3.1.2 Mesh generation

After the visualisation of the geometry in *GMSH*, a three-dimensional mesh is generated. In *GMSH* the maximum element sizes are defined via the vertices of a geometrical object. For the examine geometries, the vertices can be classified into three groups: vertices of the bounding box, vertices of inclusions and vertices of tunnelling surfaces. To handle the compromise between an as fine mesh as possible and reasonable computation times, each group of vertices get their own maximum element size. These maximum element sizes are globally defined in the ‘.geo’-file, after they were calculated with the *Python* script. The element sizes are parametrized and depend either on the bounding box length L , the inclusions radius or the radius of the tunnelling surfaces. The mesh is saved as a “.msh”-file, which will be used for the finite element calculation.

3.2 Input-file generation and MOOSE user element

In this section the input-file generation is shown. Like the geometry-file, the input-file is written with a *Python* algorithm. Therefore general *MOOSE* options have to be given in the master *Python* script and as a second source the file “tunnellingList.txt” needs to be imported. “tunnellingList.txt” contains all information about physical entities in the mesh and gap conductivities of each tunnelling junction. As shown in figure 3.2, these information are used to write all mandatory blocks of the input-file for *MOOSE*. This means the blocks “Mesh”, “Variables”, “Kernels”, boundary conditions “BCs”, “Materials”, “Executioner” and “Outputs” are written. While most of the blocks are self-explanatory, the block “Kernels” might not. In this block “pieces” of the regarded physics are implemented, which means operators or terms in the weak forms of partial differential equations [56]. In the input files generated with this algorithm simple “HeatConduction” is implemented as diffusion equation. Also *Dirichlet* boundary conditions are chosen for the top and bottom surface (z -direction) of the examined microstructures. An unit potential is applied, which means the “Variable” $pot = 1$ at the top and 0 at the bottom surface. Also, only steady-state simulations are done. After the mandatory blocks, the optional blocks are written, if they are selected. Blocks which are not necessary to execute the input-file, but might be needed to investigate a physical phenomena completely, are “AuxVariables”, “AuxKernels”,

“ThermalContact”, “Preconditioner” and “Postprocessor”. Here, the first two blocks are used to calculate the current density inside the material, while “ThermalContact” is used to enable electric conduction between two tunnelling surfaces. Therefore, *MOOSE* applies a flux between the two boundaries. In terms of tunnelling, the given gap conductivity is used to calculate the flux. As long as the emissivity parameters are 0 there are no losses. Also, a “Postprocessor” is applied to calculate the effective conductivity (see 3.3) and a “Preconditioner” to improve the convergence behaviour of the calculations. Afterwards, the *Python* script writes an input-file, which can be executed by *MOOSE*.

An important note is the fact, that the calculations for microstructure with $\eta < \eta_c$ do not converge, regardless of which executioner and preconditioner is used. This problem could not be solved, but reduced to its origin, in time. It seems, that the conductivity difference of matrix and inclusion material (magnitude $\sim 10^{21}$) is too large for microstructures, where the effective conductivity of the composite is dominated by the insulating behaviour of the matrix material. As soon as tunnelling is the dominant conduction process or the conductivity difference is reduced, the calculations for the exact same microstructures converge. A solution for future calculations with this algorithm might be the implementation of a hand-coded *Jacobian* matrix.

3.3 Homogenization

In this section a short insight to the homogenization method for the effective conductivity σ_{eff} calculation is given. It should be mentioned, that in this work only the effective conductivity in potential direction (z -direction) is considered, since only the conductivity between the contact surfaces matters.

The homogenization is implemented via “Postprocessor” in the input-file. Therefore the already implemented “HomogenizedThermalConductivity” postprocessor of *MOOSE* was adjusted by the supervisor of this work Mr. *Binbin Lin*. The given homogenization method is based on the “asymptotic expansion homogenization” model of *Hales et al.*. They homogenize a material quantity u^e , whose material behaviour follows the partial differential equation 3.1, by homogenizing the material property a_{ij} via an asymptotic expansion of quantity u^e (see eq. 3.2). Where x represent macroscale and y mesoscale information. The homogenized material property a_{ij}^H can then be calculated with equation 3.3. [58]

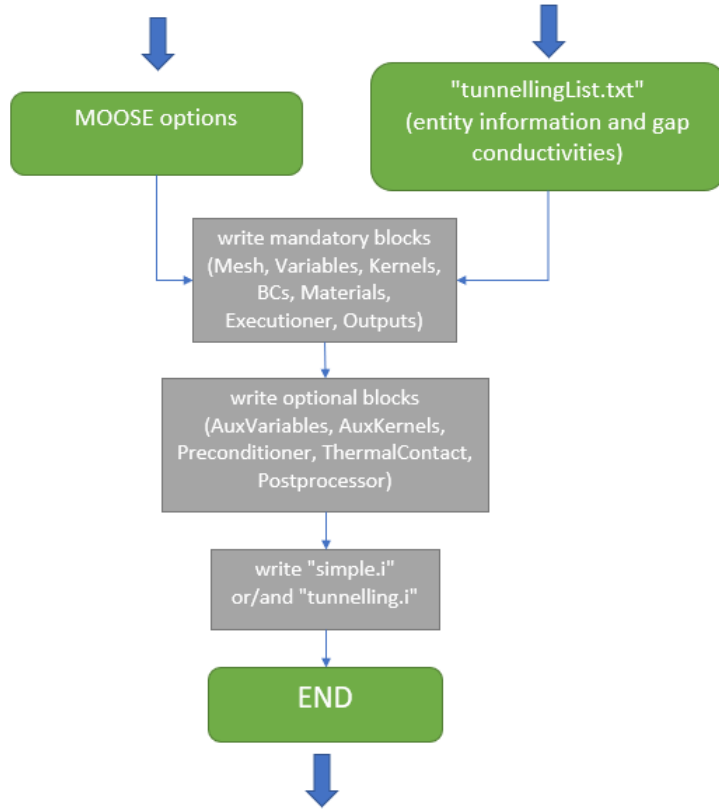


Figure 3.2: The flow chart of the input file generation is shown.

$$\frac{\partial}{\partial x_j^e} \left(a_{ij} \frac{\partial}{\partial x_j^e} \right) u^e = f \quad (3.1)$$

$$u^e = u^{(0)}(x, y) + \epsilon u^{(1)}(x, y) + \epsilon^2 u^{(2)}(x, y) + \dots \quad (3.2)$$

$$a_{ij}^H = \frac{1}{|Y|} \int_Y \left(a_{ij} + a_{ij} \frac{\partial \chi^k}{\partial y_i} \right) dy \quad (3.3)$$

Mr. *Binbin Lin* transformed this approach into a direct homogenization approach by eliminating the additional consideration of a_{ij} in equation 3.3, which leads to following equation, whose used in the present work,

$$a_{ij}^H = \frac{1}{|Y|} \int_Y \left(a_{ij} \frac{\partial \chi^k}{\partial y_i} \right) dy. \quad (3.4)$$

For the diffusion case a_{ij}^H equates the effective current density J_{eff} . And, as shown in *Awarke et al.* σ_{eff} can be calculated by considering the microstructure length L and the potential difference ΔV , which is 1 in the present work. This leads to equation 3.5. [51]

$$\sigma_{eff} = J_{eff} \frac{L}{\Delta V} \quad (3.5)$$

3.4 Calculation spanning probability

Below a description of the *Python* code for the spanning probability calculation is given. As it is shown in figure 3.3, several parameters have to be given, before the script can be executed. Similar to the geometry generation, the geometric dimensions of the microstructure, the cut-off radius and the number of inclusions have to be given. Until now, only the spanning probability of microstructures with spherical inclusions can be calculated. Depending on how precise the calculation should be, the number of iterations has to be given. Since it is a statistical approach, the higher the number of iterations, the higher the precision of the calculated value. Important to mention, that the calculation of η is dependent on λ , so the corresponding calculation, has to be edited, if $\lambda \neq \frac{1}{2}$. The first few steps of the spanning probability calculation are equal to the geometry generation, where particles are added until the desired particle number is reached and non of their cores overlap. Afterwards, the distance between the spheres is calculated and evaluated in terms of tunnelling, the result is written to a list. This list (“interactionList”) is evaluated in terms of the connections between the spheres and also the contact surfaces. If there is at least one percolation path (connection of top and bottom surface), the variable “numPaths” is increased by 1 (start value is 0). As soon as the desired number of iterations is reached, the spanning probability is calculate with equation 3.6.

$$spanningprobability(\eta, L) = \frac{numPaths}{numberOfiterations} \quad (3.6)$$

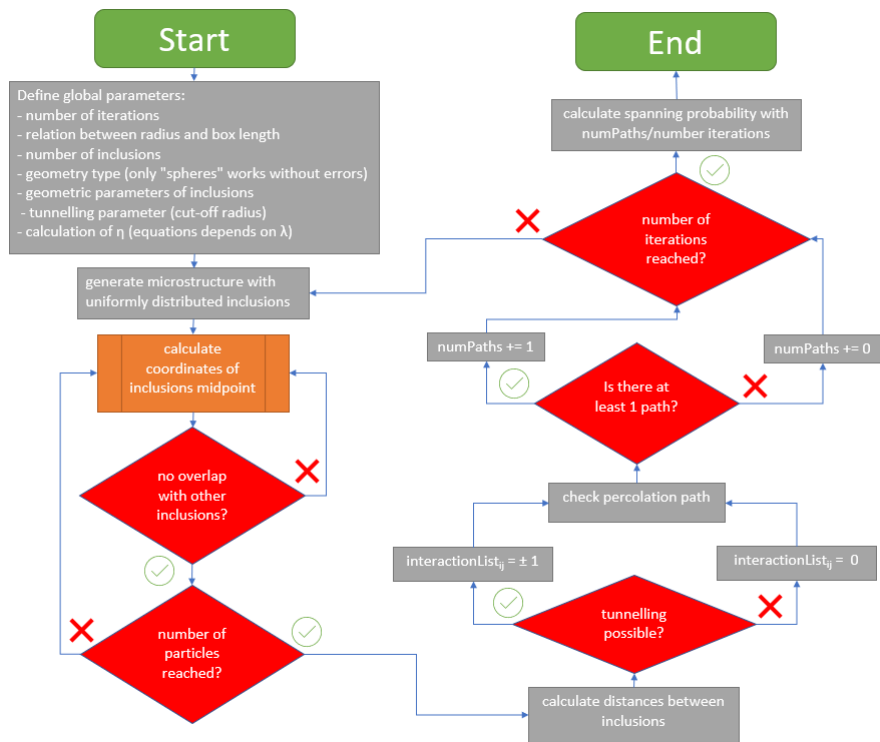


Figure 3.3: The flow chart of the spanning probability calculation is shown.

4 Results

In the following, the results of the geometry generation verification and effective conductivity calculation are presented.

At first an overview of the used parameters and its values is given in table 4.1. The core radius Φ is randomly defined, just to verify the implemented model. The characteristic tunnelling distance ξ is calculated with equation 2.35, with $\Delta E = 1.72 \text{ eV}$ as it can be determined via the electron affinity rule 4.1 [41]. Due to electron affinities of graphite $\chi_I = 4.5 \text{ eV}$ [59, 60] and PEI $\chi_M = 2.78 \text{ eV}$ [61, 62]. In addition the contact conductance σ_0 is fixed at a value of $1.0 \cdot 10^6$, which is the order of magnitude of the inclusion conductivity, but is most likely several orders of magnitude above its real value. This is done, regardless the consequence that a quantitative analysis of the effective conductivity is not possible anymore. However, such an analysis would have been difficult despite the determination of σ_0 , since there are no literature values for this material-particle shape combination. *Davidson et al.*, who used the same material combination and whose publication [63] is an origin of this work, have thin graphite flakes and graphene nanosheets as inclusions. Since these inclusions have a complete different aspect-ratio and different percolation behaviour, the values of *Davidson et al.* can not be used as reference data. Nevertheless, a qualitative analysis is still possible. Therefore, the value of σ_0 is set as large as possible, to investigate the maximal influence of the tunnelling effect.

$$\Delta E = \chi_I - \chi_M \tag{4.1}$$

Table 4.1: Geometric and material parameters for calculations in the present work (t.b.d. = to be determined).

variable	meaning	value
Φ	spheres core radius	1.0 nm
R	cut-off radius	(2Φ)
ξ	characteristic tunnelling distance	0.15 nm
L	length of bounding box	$r\Phi L \cdot \Phi$
$r\Phi L$	relation core radius and box length	(10, 15, 20, 30)
λ	penetrability coefficient	$\frac{\Phi}{\Phi+R} = \frac{1}{2}$
η	inclusion density	eq. 2.38
η_c	critical inclusion density of infinite system	t.b.d.
$\eta_c(L)$	critical inclusion density of finite system	t.b.d.
x	volume concentration	eq. 2.39
x_c	critical volume concentration	t.b.d.
σ_M	matrix conductivity	$1.0 \cdot 10^{-15} \frac{S}{m}$ [64, 65]
σ_I	inclusion conductivity	$3.0 \cdot 10^6 \frac{S}{m}$ [66]
σ_0	contact conductivity	$1.0 \cdot 10^6 \frac{S}{m}$
σ_{eff}	effective conductivity	t.b.d.

4.1 Verification of geometry generation

In order to review the geometry generation and to evaluate the generated microstructures, the same steps as done by *Johner et al.* in [14] are applied to the present algorithm. Since both generation procedures only vary by the used software, a coincidence is expected. As shown in section 3.4, spherical particles are uniformly distributed inside a bounding box, as long as they do not overlap. Afterwards, the distance between them is evaluated and it is decided whether tunnelling occurs. Concluding a percolation path analysis is done and the spanning probability is calculated. This was done for four different radius-microstructure length relations, with $r\Phi L = (10, 15, 20, 30)$. For $r\Phi L = 10$ the number of iterations was 10000, for the other three evaluations, only 1000 iterations were done. The resulting spanning probabilities for different particle densities η and the corresponding

fitting curves (following equation 2.42) are shown in figure 4.1. The spanning probabilities clearly show the expected behaviour, as they increase with increasing η . Also, the fitting functions, with their fitting parameters listed in table 4.2, approximate the probabilities well. However, the approximation of spanning probabilities for small systems and small densities is poor, especially for $\frac{L}{\Phi} = 10$. In addition, in contrast to the results of *Johner et al.*, the critical densities are shifted towards lower values. The functions and critical values of $\frac{L}{\Phi} = 30$ of the present work and $\frac{L}{\Phi} = 15$ of *Johner et al.* should coincide (consider the different meaning of Φ in [14]). However, there is a shift of η_c of about 5% towards lower values in the present work. As a reason for this purpose, the distribution functions of the particles should be considered. Also, the algorithm distributes the particles uniformly in the present work, the coordinates of a possible new particle are overwritten as soon as an overlap occurs. This leads to a change in the distribution function. In contrast, *Johner et al.* apply an additional Metropolis algorithm to relax the system and ensure uniform particle distribution. Hence, their critical density for infinite systems matches the theoretical value of 0.342 [14, 44, 67]. η_c of the present work is determined by the analysis of the fitting parameters along the equations 2.43.

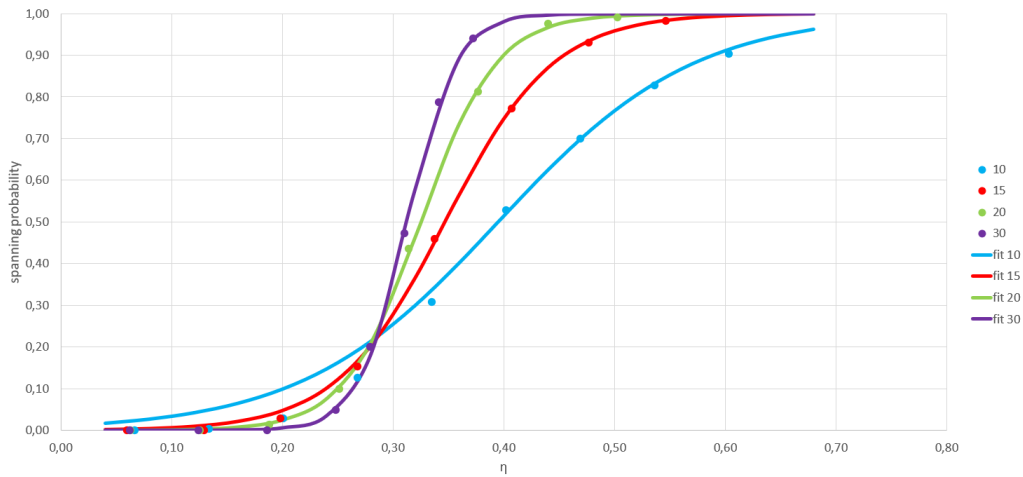


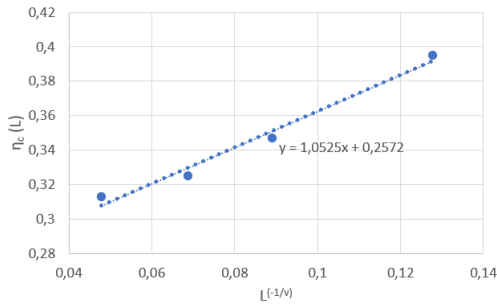
Figure 4.1: The spanning probabilities for different Φ - L relations and their corresponding fitting functions are shown.

As shown in figure 4.2 the length-independent critical density is fitted to 0.2572, which is about 8% smaller than the literature value. Despite this the correlation length exponent ν , which is the negative inverse of the gradient in figure 4.2B, coincide almost perfectly

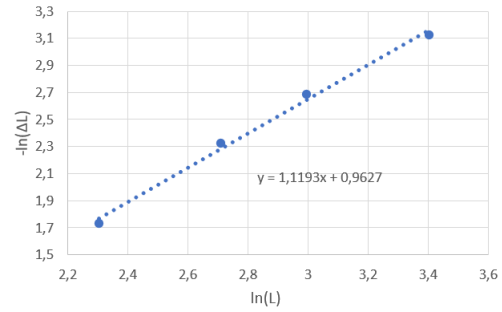
Table 4.2: Fitting parameters of fitting functions for the corresponding spanning probabilities.

$r\Phi L$	10	15	20	30
$\eta_c(L)$	0.395	0.347	0.325	0.313
ΔL	0.177	0.098	0.068	0.044

with the literature value of 0.88 [14, 50]. This leads to the result, that, even though the uniform particle distribution might not given, the algorithm is still able to generate microstructures with physically reasonable behaviour. The disturbed distribution has an higher impact on microstructures with low particle densities, since percolation paths are unlikely to occur in this density range. If the disturbance leads to an inhomogeneous distribution and clustering, percolation paths occur. Therefore the spanning probability for lower densities is increased, the length-dependent critical density $\eta_c(L)$ is reached for lower densities and leads to a shift in figure 4.1. In the following calculations the critical particle density η_c is considered to be 0.2572, since this is the predicted value for present microstructures.



(a) A



(b) B

Figure 4.2: Evaluation of η_c and correlation length exponent ν with equations 2.43, yields values of 0.2572 and 0.89, respectively.

4.2 Analysis of potential and current density distributions

In this section the potential and current density distributions of microstructure with different lengths and particle densities are evaluated regarding physical plausibility. At first the used meshes are presented in figures 4.3. As shown there, the mesh of the matrix material is almost regular, if no inclusion is close. In this case the mesh is locally refined to ensure a high quality of the results.

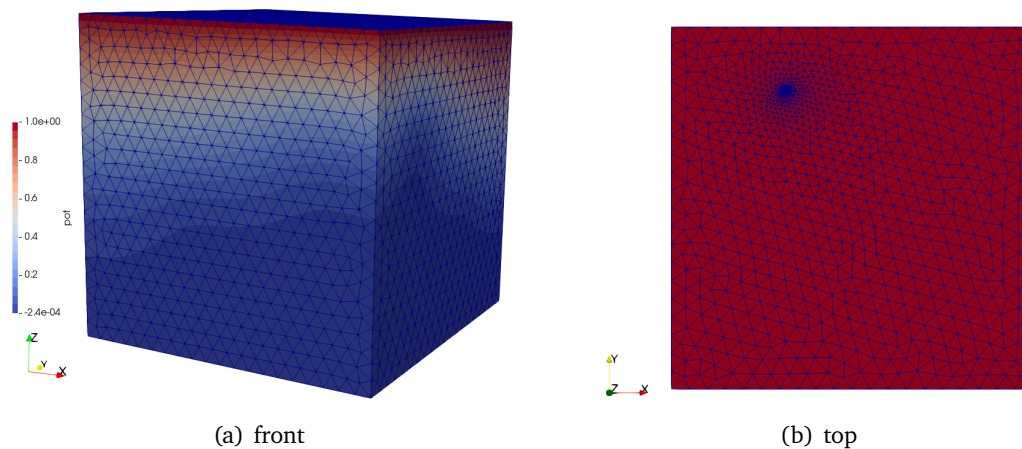


Figure 4.3: Representative meshes as front and top view.

As a next step the potential distribution inside microstructures with and without percolation paths are investigated. Representative microstructures are shown in figures 4.4. While the potential in spheres without connection to the top surface, remains 0, it changes for the other ones. If there is no percolation path the potential inside the spheres increases up to the applied value on the top contact surface. From a physical point of view, the electrons can move into the connected spheres, but not any further, since the matrix material is completely insulating. Also, particles with no connection to the top surface are isolated. If there is a percolation path, the distribution changes. The potential inside the connected spheres changes linearly with their position inside the microstructure. This is expected, since it coincides with the potential distribution for a physical connected, conducting material.

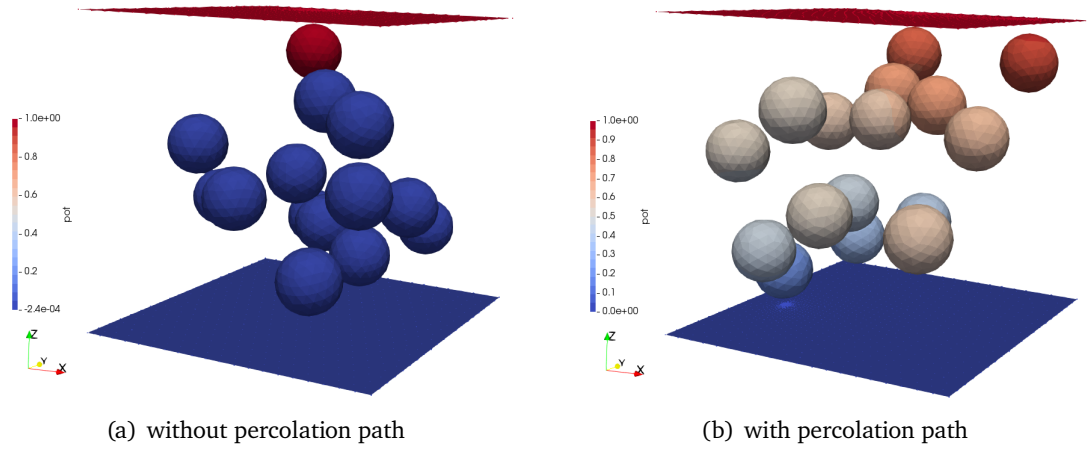


Figure 4.4: Potential distribution in representative microstructures with no percolation path (left) and with percolation path (right).

The most significance for the quality of the physical behaviour of the generate microstructure has the current density or flux distribution. Any non-physical behaviour would be visible. For better visualisation of crucial behaviour easier comparison of the different microstructures, the visualization of the current densities is limited to the range of -1 to 1 . Thus, any essential fluxes in positive z -direction are marked red and essential fluxes in negative z -direction in blue. As it is visible in the flux distribution for microstructure without percolation path (figure 4.5 left) the flux in almost every sphere is around 0 . Some areas inside the isolated particles (see figure 4.4) show high fluxes in both directions. These are numerical errors which can be ignored, since they cancel each other out. The non-isolated sphere at the top shows a similar distribution. Also, this makes physically sense, since a flux inside the sphere is applied, but no flux out of the sphere. Hence, the simulation software tries to homogenize the potential inside the sphere and the flux seems anisotropic, as seen here. In contrast, the flux distribution for a microstructure with percolation path is directional. The current density inside the inclusions is directed towards the bottom, as it is expected. Even though, there are some areas with strong fluxes in positive z -direction, they can be explained by the relative position of the tunnelling surfaces inside the inclusions and the relative orientation of the spheres. Since the tunnelling surfaces are shifted towards the spheres midpoints, there is some high conducting material between the tunnelling and the particle surface. As the *ThermalContactAction* connects only the tunnelling surfaces, electrons tunnel inside the particles and diffuse in

the surrounding material. Therefore in areas positioned above a tunnelling surface fluxes in positive z -direction occur.

Figures 4.6 assist this explanation, since the glyphs (direction of the flux) mainly point towards the negative z -direction and most of the glyphs in positive direction point in a circular way. Which indicates, that these areas are just “filled” with electrons, since there is a potential difference between the lower tunnelling surface and the higher positioned surround material.

Even though, the current density inside the matrix seemed equals 0, it is actually not. Since the matrix material has a finite conductivity, also the current density is finite (see figure 4.6 right).

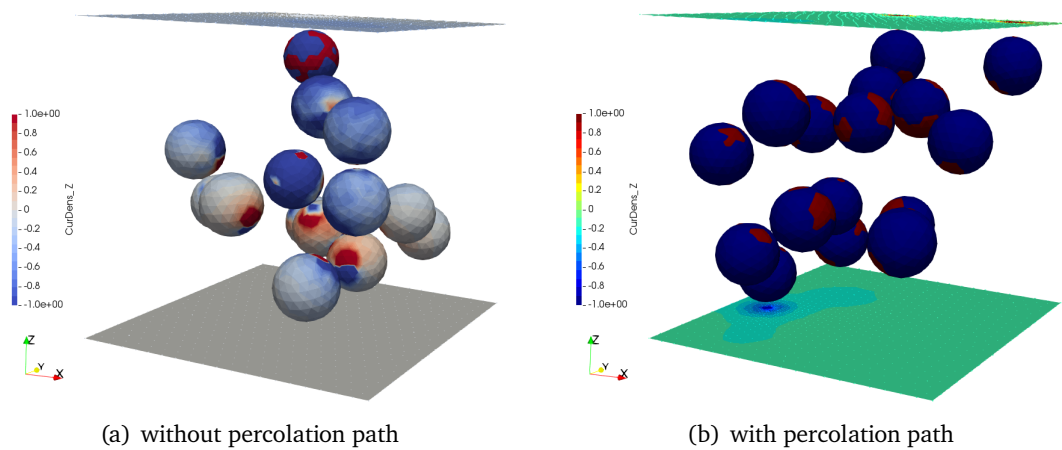


Figure 4.5: Current density distribution in representative microstructures with no percolation path (left) and with percolation path (right).

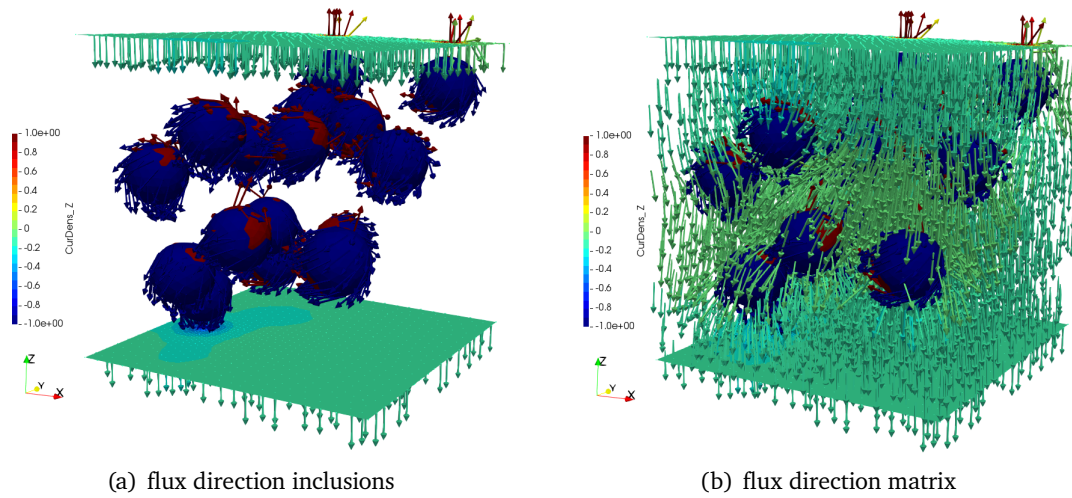


Figure 4.6: Current density direction in a microstructures with percolation path inside inclusions (left) and inside the matrix material (right).

4.3 Effective conductivities

In this section the calculated effective conductivities are presented. Since only simulations of microstructures with densities close to or higher than the percolation threshold converge and *GMSH* is not able to mesh geometries with more than 250 tunnelling junctions (the amount of geometrical entities might be too high), the amount of simulation data is low. Only the results of simulations for Φ - L relation of 10 and 20, can be evaluated. In figure 4.7 the mean values of effective conductivities relative to their particle densities are plotted. In addition the matrix and inclusion conductivities σ_M and σ_I are shown. Starting at the critical percolation threshold η_c , the effective conductivities increase drastically with increasing density, until they reach a saturation value two orders of magnitude lower than σ_I . The same behaviour observed *Ambrosetti et al.*, which is another indicator that the implemented algorithm is able to investigate composite microstructures [26].

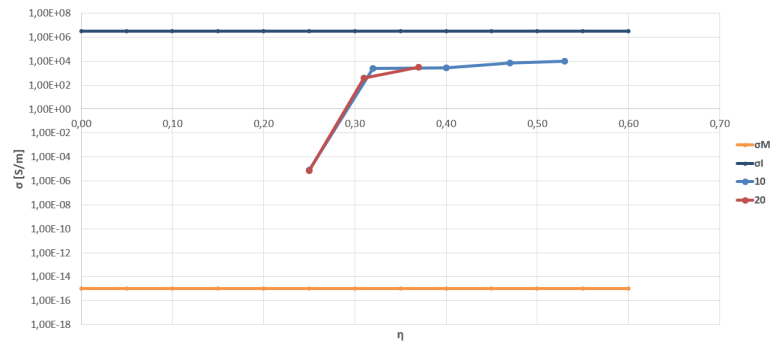


Figure 4.7: The mean values of effective conductivities for different Φ - L ratios and particle densities is shown.

5 Conclusion

As a conclusion, the present work presented an approach to implement quantum mechanical tunnelling into finite element simulation. While the functionality of the algorithm was proven, there are still options for optimization to increase the value of this user element. Especially, the choice of the software *GMSH* limited its potential, since it was not possible to mesh and subsequently calculate larger microstructures or systems with a large number of inclusions. Also overlapping particles can not be meshed, which prohibits the investigation of thin, cuboidal inclusions.

As soon as the particle distribution algorithm is optimized, it should also be possible to calculate microstructures with an exact uniform distribution. As shown, microstructures with non-uniformly distributed particles can already be investigated and lead to physical reasonable results, since it was shown, that the determining correlation length exponent ν matched the literature values.

In addition, a homogenization technique to calculate effective conductivities was successfully implemented and lead to precise and meaningful results.

Microstructures with different particle shapes should be able to investigate, since the distance calculation algorithm, even for complex shapes already exists.

Bibliography

- [1] Q. Yang et al. “Composites of functional polymeric hydrogels and porous membranes”. In: *J Mater Chem* 21.9 (2011), pp. 2783–2811. DOI: 10.1039/C0JM02234A.
- [2] F. M. Al-Oqla et al. “Natural fiber reinforced conductive polymer composites as functional materials: A review”. In: *Synthetic Met* 206 (2015), pp. 42–54. DOI: 10.1016/j.synthmet.2015.04.014.
- [3] R. B. Grubbs. “Hybrid metal–polymer composites from functional block copolymers”. In: *Journal of Polymer Science Part A: Polymer Chemistry* 43.19 (2005). DOI: 10.1002/pola.20946.
- [4] P. Thoniyot et al. “Nanoparticle–Hydrogel Composites: Concept, Design, and Applications of These Promising, Multi-Functional Materials”. In: *Adv. Sci.* 2.1-2 (2015). DOI: 10.1002/advs.201400010.
- [5] Ch. Zhang et al. “Conductive network formation and electrical properties of poly(vinylidene fluoride)-multiwalled carbon nanotube composites: Percolation and dynamic percolation”. In: *J. Appl. Polym. Sci.* 114.3 (2009). DOI: 10.1002/app.30729.
- [6] B. Zhang et al. “Percolation threshold of graphenenanosheets as conductive additives in Li₄Ti₅O₁₂ anodes of Li-ion batteries”. In: *Nanoscale* 5 (2013), pp. 2100–2106. DOI: 10.1039/c2nr33099g.
- [7] J. K. W. Sandler et al. “Ultra-low electrical percolation threshold in carbon-nanotube-epoxy composites”. In: *Polymer* 44.19 (2003), pp. 5893–5899. DOI: 10.1016/S0032-3861(03)00539-1.
- [8] W. Bauhofer and J. Z. Kovacs. “A review and analysis of electrical percolation in carbon nanotube polymer composites”. In: *Compos. Sci. Technol.* 69.10 (2009), pp. 1486–1498. DOI: 10.1016/j.compscitech.2008.06.018.
- [9] M. Monti et al. “Toward the microstructure–properties relationship in MWCNT-epoxy composites: Percolation behavior and dielectric spectroscopy”. In: *Compos. Sci. Technol.* 96 (2014), pp. 38–46. DOI: 10.1016/j.compscitech.2014.03.008.

-
- [10] R. Hashemi and G. J. Weng. “A theoretical treatment of graphene nanocomposites with percolation threshold, tunneling-assisted conductivity and microcapacitor effect in AC and DC electrical settings”. In: *Carbon* 96 (2016), pp. 474–490. DOI: 10.1016/j.carbon.2015.09.103.
- [11] F. Nilsson et al. “Simulating the effective electric conductivity of polymer composites with high aspect ratio fillers”. In: *Compos. Sci. Technol.* 132 (2016), pp. 16–23. DOI: 10.1016/j.compscitech.2016.06.008.
- [12] N. Shenogina et al. “On the lack of thermal percolation in carbon nanotube composites”. In: *Appl. Phys. Lett.* 87 (2005). DOI: 10.1063/1.2056591.
- [13] F. Kargar et al. “Thermal Percolation Threshold and Thermal Properties of Composites with High Loading of Graphene and Boron Nitride Fillers”. In: *Applied Materials Interfaces* 10.43 (2018), pp. 37555–37565. DOI: 10.1021/acsami.8b16616.
- [14] N. Johnner et al. “Transport exponent in a three-dimensional continuum tunneling-percolation model”. In: *Phys. Rev. B* 77.17 (2008). DOI: 10.1103/PhysRevB.77.174204.
- [15] C. Li, E. T. Thostenson, and T.-W. Chou. “Dominant role of tunneling resistance in the electrical conductivity of carbon nanotube-based composites”. In: *Phys. Lett. A* 91.223114 (2007). DOI: 10.1063/1.2819690.
- [16] Y. Yu, G. Song, and L. Sun. “Determinant role of tunneling resistance in electrical conductivity of polymer composites reinforced by well dispersed carbon nanotubes”. In: *J. Appl. Phys.* 108 (2010), p. 084319. DOI: 10.1063/1.3499628.
- [17] X. Zang et al. “Characteristics of the electrical percolation in carbon nanotubes-polymer nanocomposites”. In: *The Journal of Physical Chemistry C* 115.44 (2011), pp. 21685–21690.
- [18] M. Soto et al. “Modeling percolation in polymer nanocomposites by stochastic microstructuring”. In: *Materials* 8 (2015), pp. 6697–6718. DOI: doi:10.3390/ma8105334.
- [19] C. H. Seager and G. E. Pike. “Percolation and conductivity: A computer study 2”. In: *Phys. Rev. B* 10.4 (1974).
- [20] G. E. Pike and C. H. Seager. “Percolation and conductivity: A computer study. 1”. In: *Phys. Rev. B* 10.4 (1974).
- [21] S. Jung et al. “Modeling electrical percolation to optimize the electromechanical properties of CNT-polymer composites in highly stretchable fiber strain sensors”. In: *Sci. Rep.* 9 (2019), p. 20376. DOI: 10.1038/s41598-019-56940-8.

-
- [22] S. Kale et al. “Effect of filler alignment on percolation in polymer nanocomposites using tunneling-percolation model”. In: *J. Appl. Phys.* 120 (2016), p. 045105. DOI: 10.1063/1.4959610.
- [23] H. Gu, J. Wang, and C. Yu. “Three-dimensional modeling of percolation behavior of electrical conductivity in segregated network polymer nanocomposites using Monte Carlo method”. In: *Advanced in Materials* 51.1 (2016), pp. 1–8. DOI: 10.11648/j.am.20160501.11.
- [24] R. Fogelholm. “The conductivity of large percolation network samples”. In: *J. Phys. C: Solid State Phys.* 13 (1980), p. 571.
- [25] W. S. Bao et al. “Tunneling resistance and its effect on the electrical conductivity of carbon nanotube nanocomposites”. In: *J Appl Phys* 111 (2012), p. 093726. DOI: 10.1063/1.4716010.
- [26] G. Ambrosetti et al. “Electron tunneling in conductor-insulator composites with spherical fillers”. In: *J. Appl. Phys.* 106 (2009), p. 016103. DOI: 10.1063/1.3159040.
- [27] B. P. Singh et al. “Development of oxidation and corrosion resistance hydrophobic graphene oxide-polymer composite coating on copper”. In: *Surf. Coat. Technol.* 232 (2013), pp. 475–481. DOI: 10.1016/j.surfcoat.2013.06.004.
- [28] B.M. Praveen et al. “Corrosion studies of carbon nanotubes–Zn composite coating”. In: *Surf. Coat. Technol.* 201.12 (2007), pp. 5836–5842. DOI: 10.1016/j.surfcoat.2006.10.034.
- [29] X.H. Chen et al. “Corrosion behavior of carbon nanotubes–Ni composite coating”. In: *Surface and Coatings Technology* 191.2 (2005), pp. 351–356. DOI: 10.1016/j.surfcoat.2004.04.055.
- [30] L. De Broglie. “Recherches sur la théorie des Quanta”. PhD thesis. Migration - université en cours d’affectation, 1924.
- [31] H. Paul. *Introduction to quantum theory*. Cambridge University Press, 2008. DOI: 10.1017/CB09780511755644.
- [32] N. Hu et al. “Tunneling effect in a polymer-carbon nanotube nanocomposite strain sensor”. In: *Acta Mater.* 56 (2008), pp. 2929–2936. DOI: 10.1016/j.actamat.2008.02.030.
- [33] H. Lueth. *Quantum Physics in the Nanoworld*. 2nd ed. 2015. Springer International Publishing, 2015. DOI: 10.1007/978-3-319-14669-0.
- [34] O. Marti and M. R. Goncalves. “Vorlesungsskript PHYS2200.0 Atomphysik”. 2019.

-
- [35] S. M. S. Kalahroudi. “Some advancement in ionization of atoms and molecules in intermediate intensity regime using ultra-fast laser pulses”. PhD thesis. Faculte des Sciences et de Genie - Universite Laval, Quebec, 2010. DOI: 20.500.11794/22173.
- [36] M. G. Schaetzel. “Mehrphotonen-Ionisationsprozesse mit intensiven Laserpulsen”. PhD thesis. Ludwig-Maximilians Universitaet Muenchen, 2006.
- [37] F. Kleeschulte. “Analyse der Elektronenemission bei der Wechselwirkung ultrakurzer, hochintensiver, CEP-stabiler Laserpulse mit Festkoerperplasmen”. PhD thesis. Heinrich-Heine Universitaet Duesseldorf, 2017.
- [38] H. Sawada et al. “STEM imaging of 47-pm-separated atomic columns by a spherical aberration-corrected electron microscope with a 300-kV cold field emission gun”. In: *J. Electron Microsc.* 58.6 (2009), pp. 357–361. DOI: 10.1093/jmicro/dfp030.
- [39] FJ Humphreys and Brough I. “High resolution electron backscatter diffraction with a field emission gun scanning electron microscope.” In: *J. Microsc.* 195.1 (1999), pp. 6–9.
- [40] A.S. Baturin et al. “Field emission gun for X-ray tubes”. In: *Nuclear Instruments and Methods in Physics Research Section A: Accelerators, Spectrometers, Detectors and Associated Equipment* 558.1 (2006), pp. 253–255. DOI: 10.1016/j.nima.2005.11.033.
- [41] A. Klein. “Halbleitergrenzflaechen”. lecture notes. 2012.
- [42] D. Stauffer and A. Aharony. *Introduction to percolation theory*. 2nd ed. Taylor & Francis, 1992. DOI: 10.1201/9781315274386.
- [43] B. I. Halperin and S. Feng. “Differences between lattice and continuum percolation transport exponents”. In: *Phys. Rev. Lett.* 54.22 (1985).
- [44] I. Balberg. “Tunneling and nonuniversal conductivity in composite materials”. In: *Phys. Rev. Lett.* 59.12 (1987), pp. 1305–1308.
- [45] S. Vionnet-Minot et al. “Tunneling-percolation origin of nonuniversality: Theory and experiments”. In: *Phys. Rev. B* 71 (2005), p. 064201. DOI: 10.1103/PhysRevB.71.064201.
- [46] P. M. Kogut and J. P. Straley. “Distribution-induced non-universality of the percolation conductivity exponents”. In: *J. Phys. C: Solid State Phys.* 12 (1979), p. 2151.
- [47] S. Torquato, B. Lu, and J. Rubinstein. “Nearest-neighbor distribution functions in many-body systems”. In: *Phys. Rev. A* 41.4 (1990).

-
- [48] O. Stenull and H.-K. Janssen. “Conductivity of continuum percolation systems”. In: *Phys. Rev. E* 64 (2001), p. 056105. DOI: 10.1103/PhysRevE.64.056105.
- [49] C. Grimaldi et al. “Segregated tunneling-percolation model for transport nonuniversality”. In: *Phys. Rev. B* 68 (2003), p. 024207. DOI: 10.1103/PhysRevB.68.024207.
- [50] M. D. Rintoul and S. Torquato. “Precise determination of the critical threshold and exponents in a three-dimensional continuum percolation model”. In: *Journal of Physics A Mathematical General* 30.16 (1997), pp. L585–L592. DOI: 10.1088/0305-4470/30/16/005.
- [51] A. Awarke et al. “Percolation–tunneling modeling for the study of the electric conductivity in LiFePO₄ based Li-ion battery cathodes”. In: *J Power Sources* 196.1 (2011), pp. 405–411. DOI: 10.1016/j.jpowsour.2010.07.048.
- [52] E. K. Sichel, J. I. Gittleman, and P. Sheng. “Transport properties of the composite material carbon-poly(vinyl chloride)”. In: *Phys. Rev. B* 18.10 (1978), pp. 5712–5716.
- [53] P. Sheng, E. K. Sichel, and J. I. Gittleman. “Fluctuation-induced tunneling conduction in carbon-polyvinylchloride composites”. In: *The American Physical Society* 40.18 (1978).
- [54] G. Schwartz, S. Cervený, and A. J. Marzocca. “A numerical simulation of the electrical resistivity of carbon black filled rubber”. In: *Polymer* 41 (2000), pp. 6589–6595.
- [55] C. Geuzaine and J.-F. Remacle. “Gmsh: a three-dimensional finite element mesh generator with built-in pre- and post-processing facilities”. In: *International Journal for numerical methods in engineering* 79.11 (2009), pp. 1309–1331. DOI: doi.org/10.1002/nme.2579.
- [56] C. J. Permann et al. “MOOSE: Enabling massively parallel multiphysics simulation”. In: *SoftwareX* 11 (2020), p. 100430. DOI: <https://doi.org/10.1016/j.softx.2020.100430>. URL: <http://www.sciencedirect.com/science/article/pii/S2352711019302973>.
- [57] D. R. Gaston et al. “Physics-based multiscale coupling for full core nuclear reactor simulation”. In: *Annals of Nuclear Energy* 84 (2015), pp. 45–54.
- [58] J. D. Hales et al. “Asymptotic expansion homogenization for multiscale nuclear fuel analysis”. In: *Comput. Mater. Sci.* 99 (2015), pp. 290–297. DOI: 10.1016/j.commatsci.2014.12.039.
- [59] T. O. Wehling et al. “Phonon-mediated tunneling into graphene”. In: *Phys. Rev. Lett.* 101 (2008), p. 216803. DOI: 10.1103/PhysRevLett.101.216803.

-
- [60] S. J. Sque, R. Jones, and P. R. Briddon. “The transfer doping of graphite and graphene”. In: *phys. stat. sol.* 204.9 (2007), pp. 3078–3084. DOI: 10.1002/pssa.200776313.
- [61] C. Yuan et al. “Polymer molecular semiconductor all-organic composites for high-temperature dielectric energy storage”. In: *Nat Commun* 11 (2020), p. 3919. DOI: 10.1038/s41467-020-17760-x.
- [62] C. Yuan et al. “Polymer molecular semiconductor all-organic composites for high-temperature dielectric energy storage Supplementary Information”. In: *Nat Commun* 11 (2020), p. 3919. DOI: 10.1038/s41467-020-17760-x.
- [63] R. D. Davidson et al. “Tortuosity but not percolation: Design of exfoliated graphite nanocomposite coatings for extended corrosion protection of aluminium alloys”. In: *Applied Nano Materials* 2 (2019), pp. 3100–3116. DOI: 10.1021/acsanm.9b00451.
- [64] *Polyetherimid*. German. Kern GmbH Kunststoffwerke. Jan. 2021. URL: https://www.kern.de/de/technisches-datenblatt/polyetherimid-pei?n=2501_1.
- [65] *Polyetherimid PEI*. English. AZO Materials. Jan. 2021. URL: <https://www.azom.com/article.aspx?ArticleID=1883>.
- [66] A. F. Holleman. *Band 1 Grundlagen und Hauptgruppenelemente*. Ed. by N. Wiberg. De Gruyter, 2016. DOI: 10.1515/9783110495850.
- [67] C. D. Lorenz and R. M. Ziff. “Precise determination of the critical percolation threshold for the three-dimensional swiss cheese model using a growth algorithm”. In: *J. Chem. Phys.* 114.8 (2001). DOI: 10.1063/1.1338506.